

Magnetism of pure iron jarosites

Daniel Grohol, Daniel G. Nocera,* and Dimitris Papoutsakis†

Department of Chemistry, 6-335, Massachusetts Institute of Technology, 77 Massachusetts Avenue,
Cambridge, Massachusetts 02139-4307

(Received 14 May 2002; published 6 February 2003)

Stoichiometrically pure jarosites of the formula $A\text{Fe}_3(\text{OH})_6(\text{SO}_4)_2$ with $A = \text{Na}^+, \text{K}^+, \text{Rb}^+, \text{and } \text{NH}_4^+$ have been afforded by a newly developed redox-based, hydrothermal method. The jarosites exhibit an intralayer antiferromagnetic exchange interaction ($-829 \text{ K} < \Theta_{\text{CW}} < -812 \text{ K}$) and transition temperatures for long-range order (LRO) ($61 \text{ K} < T_N < 65 \text{ K}$) that are essentially insensitive to the size of the A^+ ion. A cusp at T_N in the ac susceptibility curve is frequency independent. The origin of LRO is consistent with coupling of jarosite layers exhibiting a net magnetization, which arises from an anisotropy developed, most likely, from the Dzyaloshinsky-Moriya (DM) interaction. A canted intralayer spin structure, which is a consequence of the DM interaction, is signified by a remanent magnetization ($\sim 53 \text{ K} < T_D < \sim 58 \text{ K}$), the magnitude of which depends on crystallite size. X-ray single crystal analyses of the pure Fe^{3+} jarosite compounds reveal that the *kagomé* layers are structurally invariant with those of their Cr^{3+} and V^{3+} relatives. This structural homology allows the sign and magnitude of exchange coupling within *kagomé* layers to be correlated to the different orbital parentages engendered by the M^{3+} *d*-electron count. Infrared studies show the presence of H_2O within the *kagomé* layers of alkali metal and hydronium ion Fe^{3+} jarosites prepared by conventional precipitation methods; conversely, H_2O is absent within the *kagomé* layers of jarosites prepared by the new redox-based hydrothermal methods. These results suggest that the absence of LRO in $(\text{H}_3\text{O})\text{Fe}_3(\text{OH})_6(\text{SO}_4)_2$ is due to structural and magnetic disorder arising from proton transfer from the interlayer hydronium ion to the bridging hydroxide ions of the *kagomé* layers.

DOI: 10.1103/PhysRevB.67.064401

PACS number(s): 75.50.Ee

I. INTRODUCTION

The jarosite family of minerals $A\text{Fe}_3(\text{OH})_6(\text{SO}_4)_2$,^{1–5} ($A = \text{monovalent ion}$) and its Cr^{3+} relative^{6–9} have attracted considerable attention as prominent models of a *kagomé* Heisenberg-type antiferromagnet. Extended two-dimensional *kagomé* layers comprise triangles connected through their shared vertices. The unusual magnetic property of spin frustration^{10,11} results when unpaired spins, situated at triangle corners, couple with nearest-neighbor antiferromagnetic exchange. In theory, geometric considerations imposed by the triangular spin arrangement engender an infinite number of degenerate ground states, and such a material should not display conventional long-range order (LRO).^{10–13} Notwithstanding, in all but one Fe^{3+} jarosite, LRO is observed.

LRO in *kagomé* antiferromagnets is established when the ground-state degeneracy created by spin frustration is lifted by the presence of further-neighbor exchange interactions, by anisotropy or by lattice disorder. The latter perturbation is particularly relevant to jarosites because they have been notoriously difficult to prepare in pure form. Jarosites are usually synthesized by their precipitation from hydrolyzed acidic solutions of sulfate anions and monovalent and trivalent cations.¹⁴ Under these conditions, the monovalent A^+ cations are susceptible to replacement by hydronium ions and/or the coverage of the Fe^{3+} lattice sites is incomplete; consequently, samples with magnetic site occupancies of 70–94% are obtained. Unavoidably, the magnetic behavior of these compositionally variant jarosites has been sample dependent.^{1,3} Jarosites prepared to date have shown a single magnetic-phase transition with considerable variability in the ordering temperature [$T_N = 18–65 \text{ K}$ (Refs. 1, 2, 15–19)]. In

addition, uncertainties persist as to whether a second phase transition exists at $T < T_N$, as some susceptibility¹ and solid state NMR measurements²⁰ suggest.

Among the members of the jarosite family, the hydronium jarosite $(\text{H}_3\text{O})\text{Fe}_3(\text{OH})_6(\text{SO}_4)_2$ is the singular exception in its composition and magnetism. A near complete occupancy (97%) of magnetic sites in this material is complemented by the absence of LRO, as deduced from the lack of magnetic Bragg peaks in samples at temperatures approaching 1.5 K.^{15,21–24} Moreover, the hydronium jarosite exhibits spin-glass like behavior as evidenced by a frequency dependent ac susceptibility, diverging field-cooled (FC) and zero field-cooled susceptibilities (ZFC) and a freezing temperature of $T_f \sim 15 \text{ K}$.^{2,24} These spin-glass characteristics are significantly perturbed by the dilution of the magnetic Fe^{3+} sites with nonmagnetic Ga^{3+} (Ref. 25) and Al^{3+} (Refs. 26, 27) ions.

To incisively address the issue of variant magnetic properties, as a consequence of the nonstoichiometric coverage of *kagomé* lattice sites, we sought to develop new synthetic routes that would afford pure jarosites. We have designed an approach in which the magnetic M^{3+} ions are generated in a rate-controlling redox step prior to the precipitation of the jarosite. Employing this redox-based hydrothermal approach, we have prepared a new class of highly pure and single-crystalline jarosites based on the V^{3+} ion $A\text{V}_3(\text{OH})_6(\text{SO}_4)_2$ ($A = \text{Na}^+, \text{K}^+, \text{Rb}^+, \text{Tl}^+, \text{and } \text{NH}_4^+$).²⁸ With this synthetic protocol established, we have turned our attention toward exploring the generality of the method to metal ion substitution with emphasis on the preparation of pure Fe^{3+} jarosites.

We now report the application of the redox-based hydrothermal methodology to the preparation of stoichiometrically

pure Fe^{3+} jarosites $A\text{Fe}_3(\text{OH})_6(\text{SO}_4)_2$ ($A = \text{Na}^+, \text{K}^+, \text{Rb}^+$, and NH_4^+). The obtained compounds allow us to assess whether LRO is an intrinsic property of the *kagomé* lattice of jarosites. With the insights garnered from these studies, we have also addressed the heretofore perplexing observation of the absence of LRO in the hydronium Fe^{3+} jarosite. Finally, the magnetostructural data of the Fe^{3+} jarosites reported here, in conjunction with that of the V^{3+} and Cr^{3+} jarosites, allows us to correlate between jarosite magnetism and *d*-electron count. An orbital model is presented that clarifies the origins of the exchange interactions within *kagomé* layers and the presence of LRO in spin-frustrated jarosite materials.

II. EXPERIMENTAL

The $A\text{Fe}_3(\text{OH})_6(\text{SO}_4)_2$ ($A = \text{Na}^+, \text{K}^+, \text{Rb}^+$, and NH_4^+) jarosite samples used in this study were prepared by oxidizing metallic iron in acidic solutions containing the A^+ and SO_4^{2-} ions under hydrothermal conditions. Reagent or analytical grade chemicals were obtained from commercial companies and they were used without purification. Hydrothermal reactions were carried out in 23- and 125-mL Teflon-lined pressure vessels, which were purchased from Parr Instruments. A Fisher Isotemp programmable oven with forced-air circulation was used to obtain the desired temperature profiles for hydrothermal reactions. A description follows of the detailed hydrothermal conditions under which these oxidation-reduction reactions were performed. Chemical analyses were conducted by H. Kolbe Mikroanalytisches Laboratorium.

The same procedure was used for the synthesis of each of the alkali metal jarosites. The $A_2\text{SO}_4$ salt [1.70 g (12.0 mmol) of Na_2SO_4 , 4.88 g (28.0 mmol) of K_2SO_4 , 7.47 g (28.0 mmol) of Rb_2SO_4] and 2.2 mL of H_2SO_4 (40 mmol) were dissolved in 50 mL of distilled water and transferred into the Teflon liner of a 125-mL pressure vessel. A 0.56 g piece (10 mmol) of 2-mm diameter, 99.9% iron (Aldrich) wire was added to this solution. The vessel was enclosed and placed into an oven at 200 °C for the Na_2SO_4 reaction, at 202 °C for the K_2SO_4 reaction and at 204 °C for the Rb_2SO_4 reaction. After 4 days at these elevated temperatures, the oven was cooled at 0.3 °C min^{-1} to room temperature. The yellow-orange product, which precipitated on the walls of the Teflon liner, was isolated by filtration, washed with distilled water and dried in air. Yield of $\text{NaFe}_3(\text{OH})_6(\text{SO}_4)_2$: 0.29 g (18% based on Fe). Analytically calculated for $\text{H}_6\text{NaFe}_3\text{S}_2\text{O}_{14}$: H 1.25, Na 4.74, Fe 34.57, S 13.23. Found: H 1.28, Na 4.84, Fe 34.36, S 13.17. Yield of $\text{KFe}_3(\text{OH})_6(\text{SO}_4)_2$: 0.37 g (22% based on Fe). Analytically calculated for $\text{H}_6\text{KFe}_3\text{S}_2\text{O}_{14}$: H 1.21, K 7.81, Fe 33.46, S 12.81. Found: H 1.29, K 7.68, Fe 33.41, S 12.94. Yield of $\text{RbFe}_3(\text{OH})_6(\text{SO}_4)_2$: 0.24 g (13% based on Fe). Analytically calculated for $\text{H}_6\text{RbFe}_3\text{S}_2\text{O}_{14}$: H 1.10, Rb 15.62, Fe 30.62, S 11.72. Found: H 1.19, Rb 15.68, Fe 30.48, S 11.63.

The $(\text{NH}_4)\text{Fe}_3(\text{OH})_6(\text{SO}_4)_2$ jarosite was prepared by dissolving 0.913 g of $(\text{NH}_4)_2\text{S}_2\text{O}_8$ (4.0 mmol) and 0.33 mL of H_2SO_4 (6.0 mmol) in 10 mL of distilled water. The solu-

tion was transferred into the Teflon liner of a 23-mL pressure vessel. A 0.11-g piece (2.0 mmol) of 2-mm diameter, 99.9% iron wire (Aldrich) was added to this solution. The vessel was enclosed and placed into an oven at 205 °C for 4 days. The oven was then cooled at 0.6 °C min^{-1} to room temperature. The yellow product was isolated by filtration, washed with distilled water and dried in air. Yield: 0.19 g (59% based on Fe). Analytically calculated for $\text{H}_{10}\text{NFe}_3\text{S}_2\text{O}_{14}$: H 2.10, N 2.92, Fe 34.92, S 13.37. Found: H 2.15, N 2.83, Fe 35.06, S 13.41.

A jarosite of composition $(\text{H}_3\text{O})_{0.27}\text{K}_{0.73}\text{Fe}_{2.8}(\text{OH})_{5.4}(\text{OH}_2)_{0.6}(\text{SO}_4)_2$ was obtained using the previously known precipitation techniques. 8.0 g of $\text{Fe}_2(\text{SO}_4)_3 \cdot 5\text{H}_2\text{O}$ (16 mmol) and 0.57 g of K_2SO_4 (3.3 mmol) were dissolved in 50 mL of distilled water, and transferred into the Teflon liner of a 125-mL pressure vessel. The vessel was enclosed and placed into an oven at 150 °C for 8 h. The oven was then cooled at 1 °C min^{-1} to room temperature. The yellow product was isolated by filtration, washed with distilled water and dried in air. Yield: 0.90 g (17% based on Fe and 39% based on K, which was the limiting reagent). Analytically calculated for $\text{H}_{7.4}\text{K}_{0.73}\text{Fe}_{2.8}\text{S}_2\text{O}_{14.27}$: H 1.54, K 5.89, Fe 32.25, S 13.23. Found: H 1.40, K 5.69, Fe 32.68, S 12.03.

X-ray diffraction data were collected using a Siemens three-circle single crystal diffractometer equipped with a CCD detector. All data acquisitions were carried out at -90 °C in a nitrogen stream using Mo $K\alpha$ radiation ($\lambda = 0.71073$ Å), which was wavelength selected with a single-crystal graphite monochromator. For each crystal, four data sets of 40-s frames were collected over a hemisphere of reciprocal space using ω scans and a -0.3° scan width. The data frames were integrated to *hkl* intensity, and final unit cells were calculated using the SAINT program. All structures were solved by the Patterson methods and refined using the SHELXTL v.5.03 suite of programs developed by G. M. Sheldrick and Siemens Industrial Automation, Inc., 1995.

Infrared spectra of jarosites in KBr pellets were recorded on a Nicolet Magna-IR 860 Spectrometer equipped with a KBr beam-splitter and a DTGS detector. For each spectrum, 32 scans were acquired with 4 cm^{-1} resolution over a wavelength range of 4000–400 cm^{-1} .

Magnetic susceptibility measurements of ~ 50 -mg powdered samples contained in gelatin capsules were measured using a SQUID susceptometer (Quantum Design, MPMSR2) over a 2 to 300 K temperature regime; field strengths were varied from -50 to $+50$ kOe. Prior to each measurement, residual fields were quenched. A variable nonzero background signal, observed as cooling and measuring field strengths were increased, was the primary contributing factor to the ± 30 K error of Curie-Weiss fittings. Accordingly, Weiss (Θ_{CW}) and Curie (C) constants, which were corrected for temperature independent paramagnetism and sample diamagnetic contributions as previously described,²⁹ were determined from data recorded at the same field strength of 2 kOe. Ac susceptibilities were recorded on $\text{NaFe}_3(\text{OH})_6(\text{SO}_4)_2$ under an ac field $H_{\text{ac}} = h_0 \sin(2\pi ft)$ for $h_0 = 4$ Oe and for $f = 2, 20, 200,$ and 1000 Hz.

Zero-field cooled (ZFC) measurements were performed

by cooling samples from 140 to 5 K in zero field. Data points were recorded upon warming the sample in a measuring field (H_m) that was varied from 20 Oe to 10 kOe. For field-cooled (FC) measurements, the sample was cooled from 140 to 5 K in the presence of a cooling field (H_c) that was varied from 20 Oe to 10 kOe. Experiments were run under both the conditions of $H_m = H_c$ and $H_m \neq H_c$. In the latter case, H_m was held constant at 50 Oe, while H_c was allowed to vary from 50 Oe to 10 kOe. Due to variable background effects, FC plots were normalized in high temperature regimes to their respective ZFC plot. The normalization was usually accomplished by equating χ_{\max} of the FC plot with the χ_{\max} of the ZFC plot.

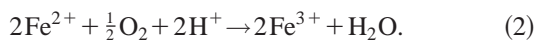
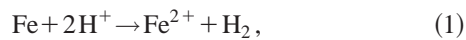
Remanent magnetization (RM) experiments were performed by cooling samples from 140 to 5 K with H_c varying from 50 Oe to 10 kOe; measurements were made upon warming from 5 to 100 K with $H_m = 0$. Background signals were recorded during such runs for $H_c = H_m = 0$ Oe, following RM measurements at different H_c . All plots were subsequently normalized by zeroing the linear part of the plot found above the transition temperature.

Particle-size dependent measurements of the remanent magnetization, were made on single crystals of $\text{KFe}_3(\text{OH})_6(\text{SO}_4)_2$ that were crushed between two glass plates. Fractions containing crystals of different sizes were then separated with the use of sieves.

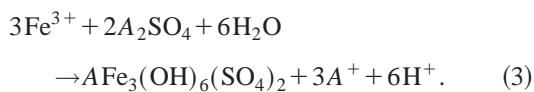
III. RESULTS

A. Synthesis

The $A\text{Fe}_3(\text{OH})_6(\text{SO}_4)_2$ ($A = \text{Na}^+, \text{K}^+, \text{Rb}^+, \text{and } \text{NH}_4^+$) jarosite samples used in this study were obtained by oxidation of iron metal in acidic solution. Under hydrothermal conditions, both elemental oxygen and protons present in the reacting solution may act as potential oxidants. In accordance with our synthetic results of the V^{3+} jarosites,²⁸ protons efficiently oxidize the metal starting material to produce solubilized metal ions and hydrogen. In the case of V^{3+} jarosite, the protons oxidize the metal ions directly to the +3 oxidation state. The Fe^{2+} oxidation state, however, is stable in acidic solution, suggesting that the production of Fe^{3+} requires oxygen as the final oxidant. This is indeed the case. If the hydrothermal reaction is performed under a nitrogen atmosphere, only a negligible quantity of jarosite is obtained. These results establish the coupled redox reaction sequence



Precipitation of jarosite proceeds according to



As we have established for the V^{3+} jarosites, the insertion of a redox step prior to precipitation of the M^{3+} ion is crucial to obtaining stoichiometrically pure and crystalline material.

For all samples used in this study, chemical analysis gave an Fe^{3+} content of $99.6 \pm 0.2\%$ and an A^+ content of $100 \pm 2\%$.

B. Structural characterization

Single crystals of the alkali metal ion derivatives of jarosite were obtained of sufficient dimensions and quality to permit their x-ray structural characterization. The pure jarosites are structurally undistinguished from previously characterized jarosite materials.^{5,28,30–36} Crystallographic data obtained from the solution of the crystal structures of the Na^+ , K^+ , and Rb^+ derivatives are listed in Table I, the atomic coordinates in Table II, and selected bond distances and angles in Table III.

The jarosite structural motif consists of layers of corner sharing $\text{Fe}_3(\text{OH})_6(\text{SO}_4)_2^-$, triangular subunits (Fig. 1), which create the characteristic *kagomé* pattern. FeO_6 octahedra composing the triangles are capped by SO_4 tetrahedra. The negative charge of each trimer subunit is balanced by a monovalent alkali ion, which also determines the interlayer distance. It is noteworthy that the size of the alkali ion does not affect the dimensions of the layer; it only affects the interlayer distance and consequently the value of the c dimension of the unit cell.

Infrared spectra of the pure Na^+ , K^+ , Rb^+ , and NH_4^+ jarosite derivatives were examined, as were the spectra of H_3O^+ and K^+ jarosite samples isolated from nonredox precipitation methods. Only results of pertinence to the magnetic properties of the jarosites are presented here; a more detailed account of the infrared spectroscopy of the pure jarosite materials will be presented elsewhere.³⁷ The IR spectrum of the K^+ derivative shown in Fig. 2(a) is exemplary of the materials obtained from our hydrothermal redox synthetic methods. A very strong peak at 3383 cm^{-1} corresponds to the O—H stretch.^{16,38,39} The energy of this O—H stretching mode increases by 25 and 33 cm^{-1} along the series $\text{NaFe}_3(\text{OH})_6(\text{SO}_4)_2 < \text{KFe}_3(\text{OH})_6(\text{SO}_4)_2 < \text{RbFe}_3(\text{OH})_6(\text{SO}_4)_2$. The (Fe—O)—H deformation mode¹⁶ appears as a strong absorption at 1005 cm^{-1} ; the location of a weak peak at 2013 cm^{-1} (the higher-energy feature of the doublet) is consistent with an overtone absorption of this mode. The antisymmetric S—O stretching modes of the sulfate anion appear at 1175 and 1085 cm^{-1} and the corresponding bending modes at 660 and 635 cm^{-1} ; the strong peaks at 509 and 472 cm^{-1} arise from the Fe—O stretching mode.¹⁶

Three prominent IR absorption features distinguish the H_3O^+ derivative from its pure alkali congeners. As shown by Fig. 2(b), the O—H stretching vibration near 3400 cm^{-1} of $(\text{H}_3\text{O})\text{Fe}_3(\text{OH})_6(\text{SO}_4)_2$ significantly broadens as does the overtone of the (Fe—O)—H deformation mode at $\sim 2000 \text{ cm}^{-1}$. More significantly, two new, weak absorptions are observed at 1640 and 1581 cm^{-1} , which correspond to H—O—H bending vibrations of the H_2O and H_3O^+ moieties, respectively.⁴⁰ In stoichiometrically pure jarosites, the O—H stretching frequencies at 3400 cm^{-1} are reduced in intensity and width, and the H—O—H bending modes are not observed. Interestingly, these distinguishing absorption features of the hydronium sample are retained in the infrared

TABLE I. Crystallographic data for the $A\text{Fe}_3(\text{OH})_6(\text{SO}_4)_2$ jarosites for $A^+ = \text{Na}^+, \text{K}^+, \text{and Rb}^+$.

	$A^+ = \text{Na}^+$	$A^+ = \text{K}^+$	$A^+ = \text{Rb}^+$
empirical formula	$\text{H}_6\text{NaFe}_3\text{S}_2\text{O}_{14}$	$\text{H}_6\text{KFe}_3\text{S}_2\text{O}_{14}$	$\text{H}_6\text{RbFe}_3\text{S}_2\text{O}_{14}$
fw	484.71	500.81	561.90
crystal system	rhombohedral	rhombohedral	rhombohedral
space group	$R\bar{3}m$	$R\bar{3}m$	$R\bar{3}m$
a (Å)	7.342(3)	7.3044(7)	7.3131(7)
c (Å)	16.605(10)	17.185(2)	17.568(3)
α (deg.)	90	90	90
γ (deg.)	120	120	120
$Z; V$ (Å ³)	3; 775.3(7)	3; 794.1(2)	3; 813.7(2)
ρ_{calc}	3.114	3.141	3.440
θ range (deg.)	3.43–23.22	3.43–23.21	3.42–23.26
scan	ω	ω	ω
temp (K)	183(2)	183(2)	183(2)
No. of refl. collected	1020	1052	1086
No. of unique refl.	162	161	169
No. of params.	26	25	26
$R1^a$ ($I > 2\sigma$, all data)	0.0325; 0.0375	0.0251; 0.0251	0.0334; 0.0338
$wR2^b$ ($I > 2\sigma$, all data)	0.0797; 0.0809	0.0581; 0.0581	0.1083; 0.1087
GOF ^c	1.268	1.323	1.237

$$^a R1 = \frac{\sum \|F_o - |F_c|\|}{\sum |F_o|}$$

$$^b wR2 = \left\{ \frac{\sum [w(F_o^2 - F_c^2)]^2}{\sum [w(F_o^2)]^2} \right\}^{1/2}$$

$$^c \text{GOF} = \left[\frac{\sum w(F_o^2 - F_c^2)^2}{(n-p)} \right]^{1/2}, \text{ where } n \text{ is the number of data and } p \text{ is the number of parameters refined.}$$

TABLE II. Atomic coordinates ($\times 10^4$) and equivalent isotropic displacement parameters (Å² $\times 10^3$) for $A\text{Fe}_3(\text{OH})_6(\text{SO}_4)_2$ for $A^+ = \text{Na}^+, \text{K}^+, \text{and Rb}^+$.

atom	x	y	z	$U(\text{eq.})^a$
Na	0	0	0	50(2)
S	0	0	3125(1)	9(1)
Fe	3333	1667	1667	9(1)
O(1)	0	0	4006(4)	10(2)
O(2)	2200(7)	1100(3)	2829(2)	12(1)
O(3)	1260(4)	2519(7)	1329(2)	11(1)
atom	x	y	z	$U(\text{eq.})^a$
K	0	0	0	14(1)
S	0	0	3087(2)	7(1)
Fe	3333	1667	1667	7(1)
O(1)	0	0	3936(4)	11(2)
O(2)	2203(7)	1102(3)	2795(2)	10(1)
O(3)	1276(3)	2553(7)	1349(2)	9(1)
atom	x	y	z	$U(\text{eq.})^a$
Rb	0	0	0	19(1)
S	0	0	3061(2)	7(1)
Fe	3333	1667	1667	6(1)
O(1)	0	0	3888(5)	12(2)
O(2)	2196(8)	1098(4)	2771(3)	9(1)
O(3)	1280(5)	2560(9)	1370(3)	9(1)

^a $U(\text{eq.})$ is defined as one third of the trace of the orthogonalized U_{ij} tensor.

spectrum of jarosite prepared by commonly used nonredox methods, i.e., by precipitation from a solution of K_2SO_4 and $\text{Fe}_2(\text{SO}_4)_3$. Figure 2(c) shows the infrared spectrum of $(\text{H}_3\text{O})_{0.27}\text{K}_{0.73}\text{Fe}_{2.8}(\text{OH})_{5.4}(\text{OH}_2)_{0.6}(\text{SO}_4)_2$ jarosite. In this spectrum, the prominent peak of the H—O—H bending mode at 1640 cm^{-1} is retained, even though the H_3O^+ and H_2O moieties are not intrinsic to the alkali metal ion derivatives of the Fe^{3+} jarosite lattice.

C. Magnetism

Magnetic properties of the jarosites were investigated by monitoring the temperature and field dependence of dc and ac magnetic susceptibilities. Figure 3 displays the temperature-dependent χ_M vs T plots for $A\text{Fe}_3(\text{OH})_6(\text{SO}_4)_2$ with $A = \text{Na}^+, \text{K}^+, \text{Rb}^+, \text{and NH}_4^+$ (ZFC mode, $H_m = 2 \text{ kOe}$). Qualitatively, all samples behave in a similar manner; χ_M increases upon cooling from room temperature to approximately 70 K, and then it rises to a sharp maximum at T_N . Below T_N , the susceptibility decreases rapidly with decreasing temperature until it slightly upturns for $T < 20 \text{ K}$. The T_N values for all the jarosite derivatives are summarized in Table IV. The ordering event characterized by T_N was also observed in ac-susceptibility measurements of the $\text{NaFe}_3(\text{OH})_6(\text{SO}_4)_2$ derivative in the range of 2–1000 Hz. The χ_M vs T plot of Fig. 4 follows the dc curve through T_N ; a single, frequency independent maximum is observed at $T_N = 61.2 \text{ K}$.

Field-dependent plots of the molar magnetization $M_M(H)$, recorded at 5 K, are linear for each of the four jarosite derivatives. Consequently, corrections to the suscep-

TABLE III. Selected bond distances (Å) and bond angles (°) for the $A\text{Fe}_3(\text{OH})_6(\text{SO}_4)_2$ jarosites for $A^+ = \text{Na}^+, \text{K}^+, \text{and Rb}^+$.

Bond	Bond distances/Å		
	$A^+ = \text{Na}^+$	$A^+ = \text{K}^+$	$A^+ = \text{Rb}^+$
A—O(2) 6×	2.961(4)	2.971(4)	2.999(5)
A—O(3) 6×	2.727(4)	2.826(4)	2.902(5)
S—O(1)	1.462(7)	1.460(7)	1.45(1)
S—O(2) 3×	1.483(4)	1.481(4)	1.481(5)
Fe—O(2) 2×	2.061(4)	2.066(4)	2.070(5)
Fe—O(3) 4×	1.994(2)	1.987(2)	1.984(2)
Angle	Bond angles/deg.		
O(1)—S—O(2) 3×	109.4(2)	109.8(2)	110.1(2)
O(2)—S—O(2) 3×	109.6(2)	109.2(2)	108.8(2)
O(2)—Fe—O(2)	180	180	180
O(2)—Fe—O(3) 4×	91.8(1)	91.8(1)	91.0(2)
O(2)—Fe—O(3) 4×	88.2(1)	88.2(1)	89.0(2)
O(3)—Fe—O(3) 2×	180	180	180
O(3)—Fe—O(3) 2×	91.8(3)	90.5(2)	90.1(3)
O(3)—Fe—O(3) 2×	88.2(3)	89.5(2)	89.9(3)

tibility to account for extrinsic impurities, the presence of which is reflected in substantial deviations from linearity in $M_M(H)$ plots at low temperature,²⁰ do not need to be applied in the jarosite samples prepared in this study. Curie-Weiss plots are linear above 150 K, and their extrapolation yields Weiss constants (Θ_{CW}) of $-810 \text{ K} \pm 30 \text{ K}$, indicative of strong intralayer antiferromagnetic interactions. We acknowledge that the application of the Curie-Weiss law is problematic because the temperatures over which magnetic susceptibility measurements were performed are much lower than the Weiss constants. However, a thematic focus of the present study is to compare the magnetic results of the pure jarosites described here to those of the jarosites of past studies. Because the majority of these past studies have used the Curie-Weiss law to obtain Θ_{CW} , we choose to do the same here. Notwithstanding, a more accurate method for treating the susceptibility of the *kagomé* lattice antiferromagnet has been described⁴¹ and applied to jarosites.⁹

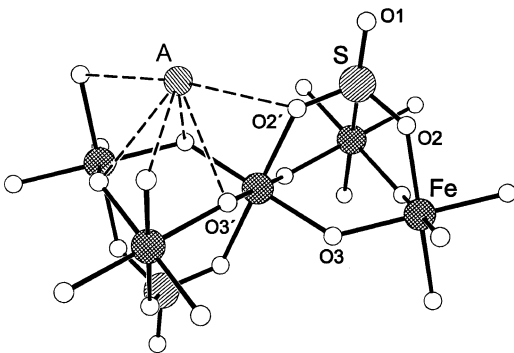


FIG. 1. The x-ray crystal structure of the magnetic subunit of the *kagomé* lattice of Fe^{3+} jarosites—the corner-sharing, $\text{Fe}_3(\text{OH})_6(\text{SO}_4)_2^-$, triangles.

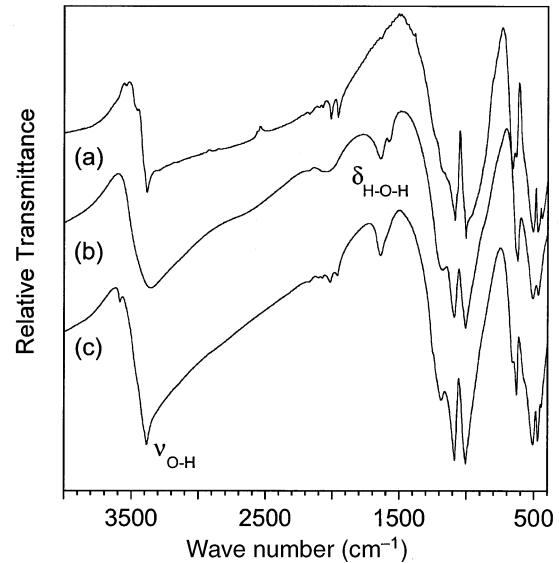


FIG. 2. IR spectra of (a) $\text{KFe}_3(\text{OH})_6(\text{SO}_4)_2$ prepared by redox-based hydrothermal methods, (b) $(\text{H}_3\text{O})\text{Fe}_3(\text{OH})_6(\text{SO}_4)_2$, and (c) the K^+ derivative of jarosite prepared by conventional nonredox precipitation methods [composition, $(\text{H}_3\text{O})_{0.27}\text{K}_{0.73}\text{Fe}_{2.8}(\text{OH})_{5.4}(\text{OH}_2)_{0.6}(\text{SO}_4)_2$].

The Θ_{CW} 's listed in Table IV are distinguished from those reported previously by their consistency. A survey of previous magnetic measurements of alkali metal derivatives of jarosite reveals Θ_{CW} 's to range from -1200 to -600 K .^{3,5,15,16,19} Under weak measuring dc-field conditions ($H_m < 50 \text{ Oe}$), a second broad maximum, which has been as-

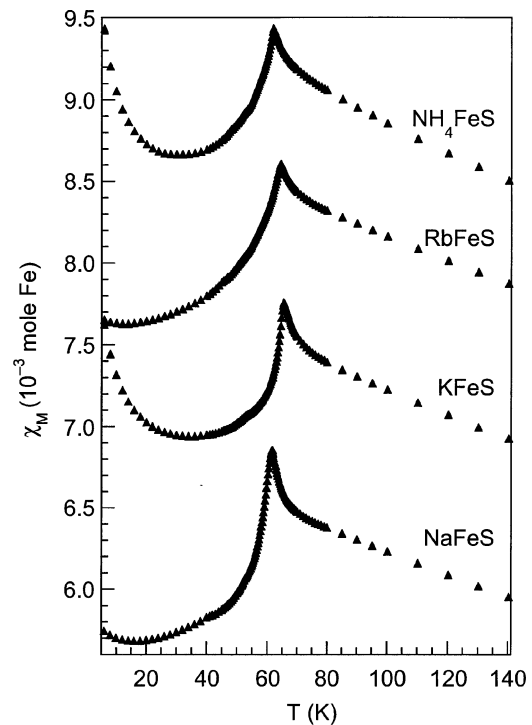


FIG. 3. Temperature dependence of χ_M (per mole of iron) vs T for $A\text{Fe}_3(\text{OH})_6(\text{SO}_4)_2$, $A^+ = \text{Na}^+, \text{K}^+, \text{Rb}^+, \text{and NH}_4^+$. For clarity, plots have been offset from each other.

TABLE IV. Magnetic parameters and interlayer space for $A\text{Fe}_3(\text{OH})_6(\text{SO}_4)$.

A^+	C^a	$\Theta_{\text{CW}}/\text{K}^a$	T_N/K	T_D/K^b	f^c	$\frac{c}{3} (=d)/\text{\AA}$
Na^+	5.91	-825	61.7	~ 58	13.5	5.535
K^+	5.77	-828	65.4	~ 53	12.7	5.728
Rb^+	5.82	-829	64.4	~ 53	12.9	5.856
NH_4^+	5.84	-812	61.8	~ 53	13.1	5.767 ^d

^aDetermined from fits of the Curie-Weiss law on data recorded over the 150–300 K temperature regime for $H_m = 2$ kOe.

^b T_D defined as the temperature where ZFC and the FC susceptibilities diverge; it also coincides with the temperature below which a remanent moment is developed.

^c $f = -\Theta_{\text{CW}}/T_N$.

^dData obtained from Ref. 1.

cribed to the onset of in-plane correlations (two-dimensional character),³ is sometimes observed between 240 and 250 K. Although the origin of this feature has not been identified, its presence accounts for discrepancies between Curie-Weiss fittings of data recorded under small and large measuring fields. An $f (= \Theta_{\text{CW}}/T_N) = 13.1 \pm 0.4$ is a signature of significant spin frustration¹⁰ imposed by the jarosite lattice. In contrast to past studies of jarosites, Curie constants (C) yield effective moments that are very close to the expected spin-only value of $5.92\mu_B$ for a high-spin Fe^{3+} ion (Table IV).

All pure jarosites display differences between their zero-field cooled (ZFC) and field-cooled (FC) magnetic susceptibilities. The χ_M vs T plots measured under ZFC and FC conditions are shown in Fig. 5 for $\text{KFe}_3(\text{OH})_6(\text{SO}_4)_2$ ($H_m = H_c = 50$ Oe); the other jarosite derivatives show similar behavior. The FC susceptibility follows the ZFC curve from the

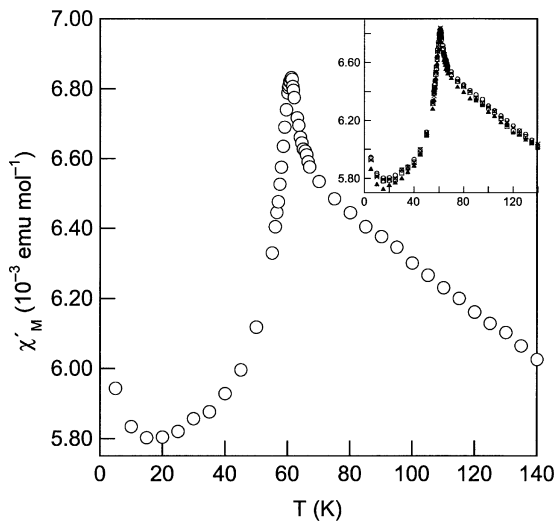


FIG. 4. Temperature dependence of the ac magnetic susceptibility χ'_M per metal center of $\text{NaFe}_3(\text{OH})_6(\text{SO}_4)_2$ under an ac field $H_{\text{ac}} = h_0 \sin(2\pi ft)$ for $h_0 = 4$ Oe and for $f = 20$ Hz. The inset displays the respective plots obtained for $f = 2$ (\square), 20 (\circ), 200 (\times), and 1000 (\blacktriangle) Hz.

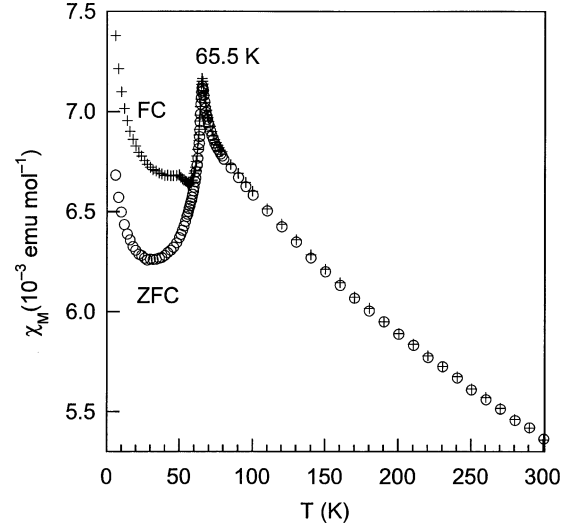


FIG. 5. The χ_M vs T plots measured under ZFC (\circ) and FC ($+$) conditions for $\text{KFe}_3(\text{OH})_6(\text{SO}_4)_2$ ($H_m = H_c = 50$ Oe).

high-temperature region through T_N , but reproducibly diverges at a temperature $T_D \sim 53$ K for $A^+ = \text{K}^+$, Rb^+ , and NH_4^+ and $T_D \sim 58$ K for $A^+ = \text{Na}^+$. As evident in Fig. 6, under identical cooling (H_c) and measuring (H_m) fields $H_c = H_m \neq 0$, the divergence between the two plots below T_D increases with decreasing field strength; the magnitude of the divergence increases with decreasing H_m (e.g., 50 Oe) and with increasing cooling fields ($H_c = 50$ Oe to 10 kOe). This variable divergence stems from the changing magnitude of the FC curve below T_D and possibly the influence that the measuring field H_m exerts on the sample. The FC data decrease in magnitude and approach those of the ZFC measurement with increasing H_m and it is not apparent above $H_m = H_c \sim 500$ Oe. When the measuring field is kept small, the

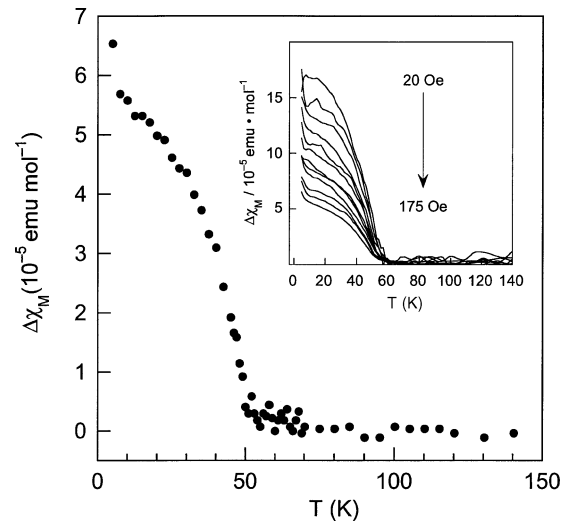


FIG. 6. Temperature dependence of $\Delta\chi_M$ (the difference between the FC and the ZFC susceptibilities), for $\text{KFe}_3(\text{OH})_6(\text{SO}_4)_2$, at $H_m = H_c = 175$ Oe. The inset displays $\Delta\chi_M(T)$ measured at field strengths ranging from 20 to 175 Oe; the arrow indicates the direction of increasing H_m .

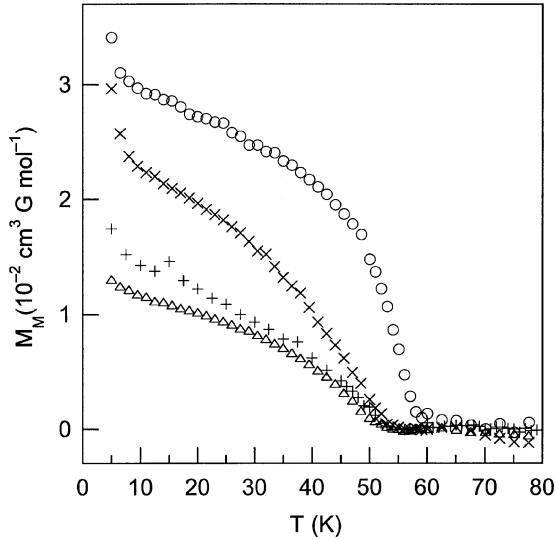


FIG. 7. Temperature dependence of remanent magnetization for $A\text{Fe}_3(\text{OH})_6(\text{SO}_4)_2$, with $A = \text{Na}^+$ (\circ) and K^+ ($+$), Rb^+ (\times) and NH_4^+ (\triangle). Samples were cooled under $H_c = 500$ Oe and measured under $H_m = 0$.

FC data constantly increase in magnitude upon increasing cooling field. Divergence between ZFC and FC curves has previously been observed for hydronium jarosite²⁴ and SCSGO.⁴²⁻⁴⁴

Powdered samples of the four jarosites exhibit a remanent magnetization (RM) when they are cooled in the presence of a magnetic field. Figure 7 displays typical RM plots recorded for samples cooled under an applied field of $H_c = 500$ Oe. Upon increasing the temperature in the absence of a magnetic field, the RM for all samples decreases until it reaches the diverging temperature T_D . Above T_D , RM disappears. As we discuss below, the RM values for the four samples depend on the particle size of the jarosite samples. For this reason, the data in Fig. 7 cannot be quantified; suffice to say, however, the magnetization saturation is $\sim 10^{-4}\%$ of that expected for fully aligned $S = \frac{5}{2}$ spins. As observed for field dependent susceptibility measurements, RM increases with increasing H_c (for $H_m = 0$) and approaches a saturation value at $H_c \sim 1$ kOe. No hysteresis was observed in the $M_M(H)$ plots under both ZFC and FC conditions utilizing different cooling fields. The observation of RM suggests the development of a weak ferromagnetic component within jarosites.

To further demonstrate the presence of weak ferromagnetism in jarosites and to delineate the conditions under which it is manifested, the following experiments were performed on $\text{NaFe}_3(\text{OH})_6(\text{SO}_4)_2$: (a) a sample was zero-field cooled from 140 K to an intermediate temperature T_α and then field-cooled ($H_c = 500$ Oe) from T_α to 5 K [this experiment is denoted FC ($T_{\text{FC}} < T_\alpha$)] and (b) the reverse experiment was performed—a sample was field-cooled ($H_c = 500$ Oe) from 140 K to T_α and then ZFC from T_α to 5 K [denoted FC ($T_\alpha < T_{\text{FC}}$)]. T_α temperatures of 100, 70, 60, 55, 45, and 30 K were selected for both experiments and $\chi_M(T)$ plots were recorded upon warming under a constant measuring field of $H_m = 50$ Oe. These types of experiments have been performed previously to uncover magnetic properties of

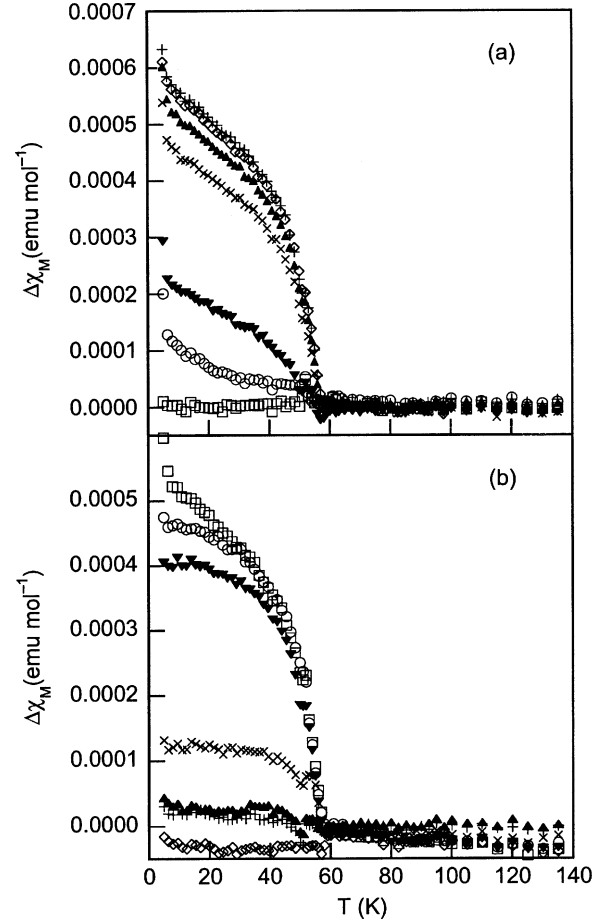


FIG. 8. Measurements of $\Delta\chi_M(T)$ of $\text{NaFe}_3(\text{OH})_6(\text{SO}_4)_2$ under the conditions of (a) zero-field cooling to an intermediate temperature T_α followed by field cooling for $T < T_\alpha$ (denoted $T_{\text{FC}} < T_\alpha$ in text) and (b) field cooling to T_α followed by zero-field cooling for $T < T_\alpha$ (denoted $T_\alpha < T_{\text{FC}}$ in text) with $H_c = 500$ Oe and $H_m = 50$ Oe, for $T_\alpha = 100$ (\diamond), 70 ($+$), 60 (\blacktriangle), 55 (\times), 45 (\blacktriangledown), 30 (\circ), and 5 K (\square). $\Delta\chi_M(T)$ is the difference between $\chi_M(T)$ measured under the conditions of (a) or (b) and $\chi_M(T)$ measured under ZFC conditions.

orthovanadates originating from the presence of canted spins.⁴⁵ Figure 8(a) displays the data from the $T_{\text{FC}} < T_\alpha$ experiment in the form of $\Delta\chi_M(T)$ [the difference of $\chi_M(T)$ measured under $T_{\text{FC}} < T_\alpha$ conditions vs $\chi_M(T)$ determined from a ZFC measurement]. A significant remanent moment develops as long as field cooling is begun at temperatures above the diverging temperature T_D . This remanent magnetization is significantly attenuated when the cooling field is applied at $T_{\text{FC}} < T_D$ [e.g., note the significant drop in $\Delta\chi_M(T)$ between $T_\alpha = 55$ K and $T_\alpha = 45$ K]. For the reverse experiment, a remanent magnetization is observed only when field cooling is applied at temperatures near or below T_D . As shown in Fig. 8(b), the ferromagnetic component is small when field cooling is removed at temperatures above T_D and increases when field cooling is maintained to $T < T_D$. Plots of the $\Delta\chi_M(T)$ for $T = 5$ K for both experiments shows that the steepest change in the remanent magnetization is observed for temperatures coincident with T_D .

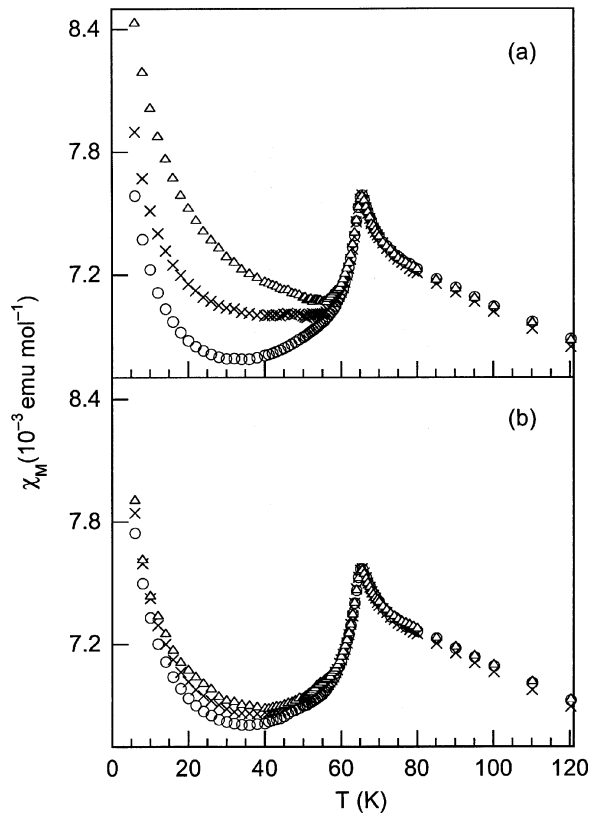


FIG. 9. Dependence of the ZFC-FC divergence on the size of $\text{KFe}_3(\text{OH})_6(\text{SO}_4)_2$ crystallites: (a) $<38\text{-}\mu\text{m}$ sieved crystallites and (b) $90\text{-}150\text{-}\mu\text{m}$ -sieved crystals for measurements performed under the conditions of $H_c=0$, $H_m=50$ Oe (\circ), $H_c=H_m=50$ Oe (\times), and $H_c=10$ kOe, $H_m=50$ Oe (\triangle).

The magnitude of the difference between the ZFC and FC measurements is related to the crystallite size of the jarosite. ZFC and FC magnetic susceptibility measurements were performed on samples of four different crystallite sizes $<38\ \mu\text{m}$, $38\text{-}63\ \mu\text{m}$, $63\text{-}90\ \mu\text{m}$, and $90\text{-}150\ \mu\text{m}$; Figure 9 shows the low temperature region of such plots for the $<38\text{-}\mu\text{m}$ - and $90\text{-}150\text{-}\mu\text{m}$ -sized materials. Zero-field cooled ($H_m=50$ Oe) and FC ($H_c=H_m=50$ Oe and $H_c=10$ kOe, $H_m=50$ Oe) traces were recorded as a function of temperature between 6 and 300 K. For the $<38\ \mu\text{m}$ sample, a significant difference appears between the ZFC and FC traces. This difference is the largest at a low temperature, and it diminishes with increasing temperature until the traces merge at ~ 55 K. This divergence between ZFC and FC traces increases and becomes more obvious with increasing H_c ; at $H_c=10$ kOe, $\Delta\chi_M$ is 8.5×10^{-4} emu mol $^{-1}$. When the particle size of $\text{KFe}_3(\text{OH})_6(\text{SO}_4)_2$ increases to $90\text{-}150\ \mu\text{m}$, the low temperature divergence between the ZFC and FC traces is significantly attenuated. When susceptibility measurements are conducted on large single crystals, the temperature-dependent ZFC and FC traces in low fields approach each other.⁴⁶ A divergence in ZFC and FC curves, similar to that observed here, has been reported for powders of the SCGO frustrated antiferromagnet,⁴²⁻⁴⁴ though the effect occurs at a much lower temperature of $T_D=3.5$ K. The magnitude of divergence on SCGO crystallite size has not

been investigated. It remains to be seen whether the behavior of ZFC-FC divergence in SCGO and jarosites is of common origin.

IV. DISCUSSION

Stoichiometrically pure jarosites display LRO at finite temperatures. The magnetic behavior of alkali metal ion members of the jarosite series is characterized by a prominent transition at T_N (see Table IV), which is in accordance with the highest T_N values previously observed either by susceptibility or neutron diffraction measurements.^{1,2,20} The observation of a frequency-independent maximum in the ac magnetic susceptibility plot precludes spin-glass behavior. Unlike the variable results of past studies of jarosites, the ordering temperature does not depend on sample preparation nor is it significantly perturbed by the size of the interlayer A^+ cation. The pure jarosite samples are further distinguished by the presence of a weak ferromagnetism associated with a secondary transition defined at T_D , the temperature at which ZFC-FC plots of the magnetic susceptibility diverge and at which the onset of a remanent magnetization is observed. Although Figs. 5 and 8 establish the ordering temperature for the ferromagnetic component and Fig. 9 clearly establishes that the magnetic properties characterized by T_D are more apparent for jarosites of small crystallite size, we currently know little else about this phenomenon. The ensuing discussion, therefore, focuses on the spin ordering characterized by T_N .

The origins of the 3D magnetic ordering in the *kagomé* layers of jarosite have previously been ascribed to three possibilities:² (1) ordering due to magnetic ion site vacancies within the lattice, (2) single-ion anisotropy, or (3) interplane coupling.

Case (1) has largely been promulgated owing to the magnetic results of the hydronium ion jarosite, which until recently has been the jarosite representative obtained in purest form and, coincidentally, is distinguished by the absence of LRO. However, the observation of 3D ordering in the highly pure jarosite samples reported here precludes case (1) as a viable cause for the presence of LRO in jarosites.

Depending on the d -electron count of the magnetic ion, single-ion anisotropy and correspondingly case (2) certainly prevails for some jarosites. For instance, the recently described V^{3+} jarosites exhibit single-ion anisotropy arising from the placement of a d^2 ion in the tetragonal crystal field of jarosite.²⁹ Ferromagnetically-coupled magnetic moments are predominantly confined to the *kagomé* plane of the V^{3+} jarosite owing to single-ion anisotropy, which is singularly most responsible for metamagnetic ordering in these materials. However, this mechanism does not translate to the d^5 electron count of the Fe^{3+} jarosites. The Fe^{3+} ion possesses a totally symmetric ${}^6A_{1g}({}^6S)$ ground state and therefore spin-orbit coupling to a first order approximation is absent.⁴⁷⁻⁴⁹ Nevertheless, spin-orbit coupling arising from a higher order mechanism will give rise to an anisotropy that can lead to interplane coupling.

In accordance with this contention, our observations are consistent with an anisotropy associated with the Dzyaloshinsky-Moriya (DM) interaction. Recent Monte

Carlo simulations suggest that the DM interaction gives rise to a net magnetization in the *kagomé* layers of Fe^{3+} jarosites.⁵⁰ In- and out-of-plane spin interactions defined by DM parameters D_p and D_z , respectively, result from the tilting of the elongated FeO_6 octahedra composing $\text{Fe}_3(\text{OH})_6(\text{SO}_4)_2^-$ triangular subunits. For jarosites, a critical region of D_z/D_p value, which depends on the intralayer interaction J , dictate a canted spin arrangement with the out-of-plane spins ferromagnetically aligned. The canted structure leads to ordering with a critical temperature that depends intrinsically on the angle between the DM vector and the *kagomé* plane. In the past, a ferromagnetic component has been observed in only two compounds of the Fe^{3+} and Cr^{3+} jarosite family. The RM experiments of Figs. 5 and 8, however, reveal a weak ferromagnetism that develops from the canted spins for *all* four jarosites and it is preserved after 3D ordering is established. Consistent with these experimental and theoretical treatments, single-crystal magnetic susceptibility measurements establish that the 3D ordering event corresponding to T_N is orthogonal to the *kagomé* layers.⁴⁶ These results conform to a proposal of Inami *et al.*² that a spin umbrella structure generates a net moment for each *kagomé* plane, which may couple antiferromagnetically to its neighboring layers.

The attribution of LRO to ordering within the *kagomé* layers of jarosites is satisfying from several perspectives. First, the consistency of the T_N values across the $\text{AFe}_3(\text{OH})_6(\text{SO}_4)_2$ series is concordant with the structural properties of the jarosite series summarized in Table III. The similarity of the bond lengths and angles of $\text{Fe}_3^{\text{III}}(\mu\text{-OH})_3$ triangles for the different series members presages constant intralayer exchange and DM interactions. The interlayer spacing of the $\text{AFe}_3(\text{OH})_6(\text{SO}_4)_2$ compounds increases marginally with the increasing size of the monovalent cation along the series $\text{Na}^+ < \text{K}^+ \sim \text{NH}_4^+ < \text{Rb}^+$. Therefore interlayer coupling should vary little across the A^+ series of Fe^{3+} jarosites. Accordingly, T_N should be relatively constant across the series, as we observe.

Second, the trend in the ordering temperature follows the strength of the intralayer interaction of Cr^{3+} jarosites [$T_N \sim 1.7$ (Ref. 7)–4 K (Ref. 8)] relative to their Fe^{3+} counterparts. Though the interlayer interaction should be invariant for A^+ analogs of Cr^{3+} and Fe^{3+} jarosites (due to identical interlayer distances for materials of a given A^+ ion, see Table III), the strength of antiferromagnetic coupling within the triangular *kagomé* lattices is notably disparate for these transition metal analogs. As predicted by Goodenough-Kanamori rules,^{51–53} the large and negative values of Θ_{CW} for the Fe^{3+} jarosites is consistent with strong antiferromagnetic coupling arising from a superexchange pathway comprising the metal $d_{x^2-y^2}$ orbitals and μ -hydroxy p orbitals of the $\text{Fe}_3^{\text{III}}(\mu\text{-OH})_3$ triangles of the *kagomé* layer.⁴ The σ -type orbital overlap of the $d_{x^2-y^2}-p(\text{O})-d_{x^2-y^2}$ superexchange pathway in the Fe^{3+} jarosites is significantly greater than the less directional orbital overlap of the $d_{xy}-p(\text{O})-d_{xy}$ superexchange pathway in Cr^{3+} jarosites. This weaker antiferromagnetic interaction in the Cr^{3+} jarosite is reflected in the smaller value of $\Theta_{\text{CW}} = -67$ K. Consequently, the observa-

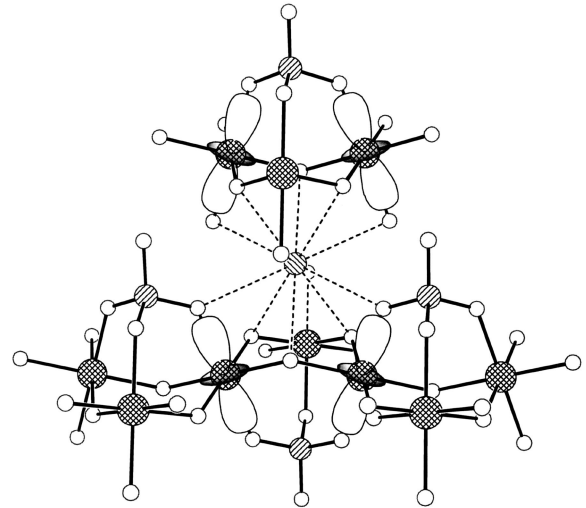


FIG. 10. A structural subunit of the jarosite lattice highlighting the icosahedral coordination sphere of the A^+ ion (the connectivity of which is shown by the dashed lines). The overlay indicates the orientation of d_{z^2} orbitals of M^{3+} ions in neighboring layers. The sphere coding of the atoms is presented in Fig. 1.

tion of a smaller T_N for Cr^{3+} jarosite appears to be a direct outcome of a more feeble exchange interaction within its *kagomé* layers.

Third, the observations reported here are in conformance with the emerging theme for LRO in jarosites. Namely, ordering within the *kagomé* layers is an important determinant of LRO, regardless of the nature of the intralayer exchange interaction. In the V^{3+} jarosites, ferromagnetic exchange is observed within *kagomé* layers and antiferromagnetic coupling of these layers results in metamagnetism; it is the ferromagnetic ordering within the layer that provides the impetus for the antiferromagnetic 3D transition.^{29,54} Thus, the critical 3D ordering temperatures of the V^{3+} metamagnet and $\text{Fe}^{3+}/\text{Cr}^{3+}$ spin frustrated antiferromagnets are dictated by the 2D exchange interaction within the *kagomé* layers, despite the fundamental differences in the sign of the interaction.

Spin-dimensionality crossover in quasi-2D systems emerges from even the most rudimentary treatments of low-dimensional magnetism.⁵⁵ Interplane coupling may be sustained by a dipolar interaction of spins between layers. Though dipolar coupling between the individual spins of different layers is typically too small to be significant, it is the dipolar coupling between spin arrays correlated on the 2D length scale that leads to 3D order.⁵⁶ This principal mechanism for magnetic communication between layers may be further augmented by *interlayer* superexchange. Of the transition metal-based orbitals that can participate in interlayer superexchange between the *kagomé* layers, d_{z^2} is preeminent. As schematically represented in Fig. 10, the d_{z^2} orbitals are directed toward neighboring layers owing to the orientation of the orbital along the elongated axis of the tetragonally distorted FeO_6 octahedron. The spins of the electrons residing in the d_{z^2} orbitals of neighboring layers may communicate along two distinct pathways. One

pathway involves the A^+ cation, which resides in a high symmetry icosahedral coordination sphere (Fig. 10) composed of six oxygens O(2) from the pyramidal base of sulfate capping groups and six oxygens O(3) from the bridging hydroxyl groups. $AM^{3+}-O(2,3)-A^+-O(2,3)-M^{3+}$ pathway connects magnetic M^{3+} sites through the interlayer A^+ cation. A second, more circuitous pathway, $M^{3+}-O(2)-S-O(1)\cdots H-O(3)-M^{3+}$, bypasses the alkali ion and includes the sulfate anion. This six-bond pathway contains one hydrogen bond, which is structurally subsumed by the O(3)—O(1) distance. Since hydrogen bonds may be effective in mediating magnetic exchange in layered systems,⁵⁷ either of the two potential pathways are viable alternatives. We note that the ordering temperatures for the four jarosites are almost identical even though the NH_4^+ derivative possesses only six-bond superexchange pathways. A longer pathway should engender a weaker superexchange interaction; accordingly, the interlayer coupling reflected in T_N should be stronger in the alkali metal ion representatives. The similarity of T_N for jarosites with alkali metal and NH_4^+ interlayer cations, therefore, suggests that the four-bond pathway does not contribute to interlayer superexchange. Yet, inasmuch as the interlayer distances of the jarosites with NH_4^+ and alkali metal ions are similar, it is difficult to unequivocally distinguish between four-bond and six-bond pathways.

Further insights into the magnetic properties of jarosites may be gleaned by considering the d -electron count of the known V^{3+} , Cr^{3+} , and Fe^{3+} jarosites and their yet unprepared Ti^{3+} and Mn^{3+} relatives. The contributions of stereo-electronic factors to observed magnetic properties are generally difficult to isolate since magnetism responds to small structural changes in the local coordination environment of the magnetic ions. But this is not the case for the *kagomé* lattice of jarosites. As we have previously discussed,^{28,29} the intralayer framework of the *kagomé* lattice of jarosite is structurally unaltered with d -electron count and with different A^+ ions: (i) equatorial and axial $M^{3+}-O$ bond distances are almost constant, differing by less than ~ 0.02 Å, (ii) the dimensions of the capping sulfate anion remain unperturbed across the series, and (iii) the $M^{3+}-O(3)-M^{3+}$ and related $O-M^{3+}-O$ in-plane and out-of-plane angles vary by $< \sim 2^\circ$ for all $AM_3(OH)_6(SO_4)_2$ compounds. This structural homology of jarosites offers the possibility to correlate the sign and magnitude of exchange interaction within isostructural *kagomé* layers to different orbital parentages engendered by the M^{3+} d -electron count.

Figure 11 depicts the standard magnetic properties of the known first row transition metal jarosites together with the d -electron occupancy of the crystal field energy level diagram. Axial elongation of the M^{3+} octahedron lifts the degeneracy of the t_{2g} and e_g orbital sets of an octahedral (O_h) crystal field. In the D_{4h} point group of the axially elongated crystal field of jarosites, the t_{2g} orbital set splits into a lower energy, doubly degenerate $e_g(d_{xz}, d_{yz})$ orbital set and an empty, singly degenerate $b_{2g}(d_{xy})$ orbital; the e_g orbital set splits into a lower energy d_{z^2} orbital and higher energy $d_{x^2-y^2}$ orbital. The two d -electrons of V^{3+} jarosite occupy

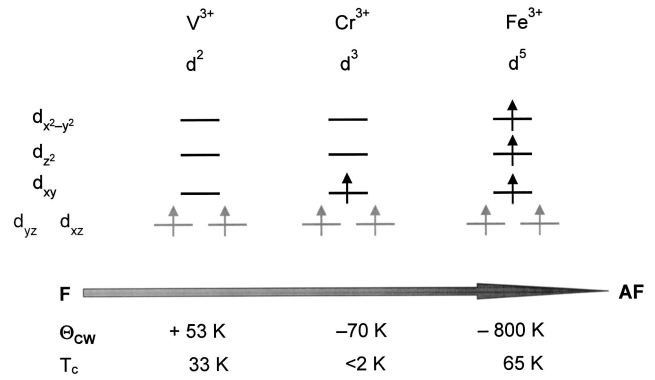


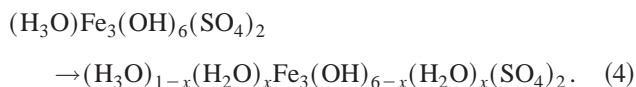
FIG. 11. The correlation between magnetic properties of jarosites and the d -orbital occupancy of the M^{3+} ion in the tetragonal crystal field.

the $e_g(d_{xz}, d_{yz})$ orbital. The positive Θ_{CW} of V^{3+} jarosite reveals that a π -symmetry pathway, composed of the interaction of the $e_g(d_{xz}, d_{yz})$ orbital set with the p orbital of the bridging hydroxide, leads to ferromagnetic exchange. When an additional electron is added to the crystal field diagram, the sign of the nearest-neighbor magnetic coupling changes. Occupation of the metal d_{xy} orbitals in Cr^{3+} jarosites leads to a dominant antiferromagnetic exchange term that overwhelms the ferromagnetic contribution of the $d\pi-p-d\pi$ pathway. Placement of two more electrons in the d_{z^2} and $d_{x^2-y^2}$ orbitals of Fe^{3+} jarosite increases this antiferromagnetic exchange interaction within the *kagomé* lattice by more than an order of magnitude. Since the overlap between the d_{z^2} orbitals and the p orbitals of the bridging hydroxide is small, the contribution of the d_{z^2} orbitals to the overall antiferromagnetic exchange pathway in plane should be insignificant. Rather, as mentioned above, the $d_{x^2-y^2}$ is responsible for the large in-plane superexchange interaction and the d_{z^2} orbital can contribute in a secondary way to the 3D ordering via a superexchange pathway orthogonal to the *kagomé* layers.

Two interesting predictions emerge from the orbital picture of Fig. 11. First, it is unlikely that the *kagomé* lattice of d^1 jarosites will possess an antiferromagnetic $S = \frac{1}{2}$ ground state, which would be important for examining the resonance valence bond model and more generally quantum disorder in spin frustrated systems.⁵⁸ The single electron of a Ti^{3+} ion in the $M_3^{\text{III}}(\mu-OH)_3$ triangles of jarosite will reside in the $e_g(d_{xz}, d_{yz})$ orbital set, which will most likely support a ferromagnetic exchange interaction and not the antiferromagnetic one required for spin frustration. However, this electronic structure may be perturbed by a Jahn-Teller distortion, making it *a priori* difficult to predict the exchange interaction for a nondegenerate $S = \frac{1}{2}$ ground state. If an antiferromagnetic ground state does not prevail, then a spin-frustrated $S = \frac{1}{2}$ ground state will have to be realized in other triangular lattices such as that of $NaTiO_2$;^{59,60} but this material will have to be prepared in pure form before reliable magnetism studies may be undertaken. Secondly, the yet unprepared Mn^{3+} jarosite will be important for assessing intralayer and interlayer couplings in jarosite systems. The Mn^{3+} jarosite will differ from its Cr^{3+} counterpart only by the population

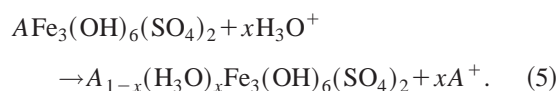
of d_{z^2} orbital. Since the contribution of d_{z^2} to the in-plane superexchange pathway is assumed to be negligible, similar Weiss constants should be observed for the Cr^{3+} (d^3) and Mn^{3+} (d^4) systems. If a superexchange pathway involving d_{z^2} is unimportant, then T_N for Cr^{3+} and Mn^{3+} jarosites will be similar. Conversely, if d_{z^2} does contribute to an out-of-plane superexchange pathway, then the 3D ordering temperature of Mn^{3+} jarosite will be greater than that of Cr^{3+} jarosite. The challenge here will be the stabilization of the Mn^{3+} oxidation state in the jarosite lattice. Thermodynamic potentials favor the disproportionation of Mn^{3+} to the Mn^{2+} and Mn^{4+} oxidation states. Thus, nonaqueous solvothermal methods will likely need to be developed for the preparation of Mn^{3+} jarosites by redox-based strategies akin to the ones reported herein.

Finally, we address the perplexing phenomenon uncovered in several past studies of jarosites—the absence of LRO in $(\text{H}_3\text{O})\text{Fe}_3(\text{OH})_6(\text{SO}_4)_2$. As mentioned above, the results of the pure jarosites presented here preclude the possibility that the absence of LRO correlates with high lattice coverage, which has approached 97% in hydronium jarosite. In this compound, hydronium ions reside in the A^+ lattice sites between layers. Weak hydrogen bonding to intralayer hydroxyl and sulfate oxygen groups is assumed,³⁸ although the H(D) atoms of hydronium have not been located in neutron diffraction studies owing to their disorder. Rather, the ion has been treated as a rigid body with bond angles and lengths defined by hydronium perchlorate. Regardless of the precise orientation of the H atoms of the hydronium, the six hydroxyl groups of the $M_3^{\text{III}}(\mu\text{-OH})_3$ triangles are in the immediate vicinity of each hydronium ion. Taken together with the large thermodynamic driving force for $\text{H}_3\text{O}^+ \text{-OH}^-$ acid-base reaction, proton transfer from the interlayer hydronium ion to the bridging hydroxyls is favored,

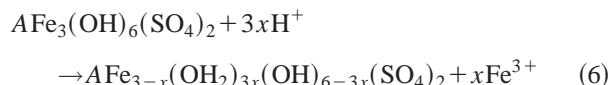


Direct evidence for this proton transfer comes from a comparison of the infrared spectra of Fe^{3+} jarosites prepared by the new redox-based methods to those of materials obtained from the conventional precipitation methods employed previous to this study. As shown by the dashed line of Fig. 2, the IR spectra of $\text{KFe}_3(\text{OH})_6(\text{SO}_4)_2$ and $(\text{H}_3\text{O})\text{Fe}_3(\text{OH})_6(\text{SO}_4)_2$ prepared by nonredox methods exhibit an absorption corresponding to the H—O—H bending mode of the H_2O molecule. In stoichiometrically pure jarosites, water is absent in the lattice and consequently this absorption is not observed; the absorption of the O—H symmetric vibration in the $3300\text{--}3400\text{ cm}^{-1}$ region is reduced in intensity and width.

The results of Fig. 2 clearly indicate the presence of water in jarosites prepared by conventional nonredox methods. The proclivity of H_3O^+ to replace the A^+ cations has been long known and this substitution has been ascribed as a primary source for “impurity” contamination in jarosites⁶¹



Ensuing proton transfer as described for the end member of the series ($x=1$, hydronium Fe^{3+} jarosite) in reaction (4) will produce the water observed in the infrared spectrum of Fig. 2. A second source of water in the jarosite lattice arises from the maintenance of charge balance within a *kagomé* lattice possessing M^{3+} site vacancies. As proposed by Kubisz⁶¹ and observed by us in the preparation of V^{3+} jarosites by conventional precipitation methods,²⁸ protonation of OH^- by H^+ to form H_2O ,



will prevent the accrual of negative charge on *kagomé* layers possessing M^{3+} site vacancies. We contend, based on the spectra of Fig. 2, that both the intrinsic and extrinsic proton transfer mechanisms described by reactions (4) and (6) respectively, prevail for the hydronium ion jarosite and more generally for any A^+ jarosite prepared by non-redox precipitation methods. In addition to these infrared data, we also note that direct spectroscopic evidence for the presence of D_3O^+ , D_2O , and OD^- in hydronium jarosite has been established previously by ^2H NMR spectroscopy.³⁸ However, the consequences of this longstanding NMR study have not fully been appreciated in the consideration of the absence of LRO in hydronium jarosite.

Proton-transfer reactions (4) and (6) have significant implications on the magnetic properties of jarosites, particularly as they pertain to LRO. First, proton transfer will influence the primary intralayer exchange pathway. A significant decrease in the strength of magnetic exchange between metal centers accompanies the protonation of an oxo ligand bridging bimetallic centers.^{62,63} In view of the foregoing model in which interlayer exchange drives 3D ordering, protonation of the hydroxyl group mediating the nearest neighbor magnetic exchange will inevitably lead to a decrease in nearest neighbor exchange and consequently to depressed T_N 's in Fe^{3+} jarosites. Secondly, proton transfer will be a disordered chemical event in the jarosite lattice. Inasmuch as structural disorder is capable of inducing spin-glass behavior,^{64,65} we believe that the spin-glass-like properties of $(\text{H}_3\text{O})\text{Fe}_3(\text{OH})_6(\text{SO}_4)_2$ are due to structural and attendant magnetic disorder caused by proton transfer reactions (4) and (6).

V. CONCLUSIONS

Pure and stoichiometric Fe^{3+} jarosites have been prepared by newly developed hydrothermal redox methods. The success of the synthetic approach relies on the insertion of a redox reaction to control the production of Fe^{3+} prior to the coprecipitation of the ion with constituent A^+ , SO_4^{2-} , and OH^- ions to afford the layered *kagomé* lattice. Lattice coverages of the magnetic and interlayer ions for the $A\text{Fe}_3(\text{OH})_6(\text{SO}_4)_2$ ($A = \text{Na}^+$, K^+ , Rb^+ , and NH_4^+) family

of jarosites were $>99\%$ for each sample. All four derivatives display LRO characterized by an essentially invariant T_N , establishing that the complete coverage of the triangular lattice of jarosites with magnetic ions does not lead to spin-glass behavior. The 3D ordering observed in the pure Fe^{3+} jarosites is consistent with interlayer coupling of a net magnetization engendered from a DM interaction among magnetic sites within the *kagomé* layers. We contend that the absence of LRO in jarosites such as $(\text{H}_3\text{O})\text{Fe}_3(\text{OH})_6(\text{SO}_4)_2$ is due to disorder induced by proton transfer from the interlayer hydronium ion to the bridging hydroxide ions. Protonation of the μ -hydroxo bridge to afford a μ -aquo bridge is manifested not only in structural disorder, but in magnetic disorder as well, derived from disparate nearest neighbor exchange coupling constants among metal centers bridged by H_2O vs OH^- .

An invariant Weiss constant of -810 K for all four members of the series indicates a structurally homologous Fe^{3+} jarosite series, which is confirmed by single crystal x-ray crystallography. This structural homology permits us to isolate the effect of d -electron count on the magnetic properties of jarosites. A comparison of the magnetic properties of V^{3+} , Cr^{3+} , and Fe^{3+} congeners, reveals the following relationship between observed magnetic properties and d -orbital occupancy in the tetragonal crystal field of jarosites $e_g(d_{xz}, d_{yz}) \Rightarrow$ moderate in-plane ferromagnetic exchange, $b_{2g}(d_{xy}) \Rightarrow$ moderate in-plane antiferromagnetic exchange of significant strength to overwhelm the ferromagnetic coupling of the superexchange pathway involving the $e_g(d_{xz}, d_{yz})$ or-

bital set, $a_{1g}(d_{z^2}) \Rightarrow$ potential secondary role in 3D ordering via a superexchange pathway that is orthogonal to *kagomé* layers, and $b_{1g}(d_{x^2-y^2}) \Rightarrow$ very strong in-plane antiferromagnetic exchange.

Our new hydrothermal synthetic methods afford pure Fe^{3+} jarosites, which have allowed us to address several issues pertaining to the magnetism of spin frustration in the *kagomé* lattice of jarosites. However, many other issues remain unresolved. These include the precise nature of in-plane and interplane coupling, the existence of SRO within the 2D *kagomé* layers, the dependence of disparate ZFC and FC behavior and remanent magnetization on crystallite size. Many of these issues may directly be interrogated with elastic and inelastic neutron scattering experiments. These studies are ongoing, enabled by our recent success in obtaining large single crystals of the Fe^{3+} jarosites from the new synthetic methods reported here.

ACKNOWLEDGMENTS

We thank Dr. Young Lee of the MIT Department of Physics for enlightening discussions and Dr. Fang Cheng Chou for technical assistance in performing magnetism measurements. Financial support for this work was provided by the National Science Foundation (Grant No. DMR-9311597) and by a seed grant from the MIT Center for Materials Science and Engineering Research, a MRSEC Program of the National Science Foundation (Grant No. DMR-9808941).

*Author to whom correspondence should be addressed. Electronic address: nocera@mit.edu

[†]Present address: Novartis Pharmaceuticals, One Health Plaza, East Hanover, NJ 07936.

¹A. S. Wills, A. Harrison, C. Ritter, and R. I. Smith, *Phys. Rev. B* **61**, 6156 (2000).

²T. Inami, M. Nishiyama, S. Maegawa, and Y. Oka, *Phys. Rev. B* **61**, 12 181 (2000).

³A. S. Wills and A. Harrison, *J. Chem. Soc., Faraday Trans.* **92**, 2161 (1996).

⁴M. G. Townsend, G. Longworth, and E. Roudaut, *Phys. Rev. B* **33**, 4919 (1986).

⁵M. Takano, T. Shinjo, and T. Takada, *J. Phys. Soc. Jpn.* **30**, 1049 (1971).

⁶A. Keren, K. Kojima, L. P. Le, G. M. Luke, W. D. Wu, Y. J. Uemura, M. Takano, H. Dabkowska, and M. J. P. Gingras, *Phys. Rev. B* **53**, 6451 (1996).

⁷S.-H. Lee, C. Broholm, M. F. Collins, L. Heller, A. P. Ramirez, Ch. Kloc, E. Bucher, R. W. Erwin, and N. Lacey, *Phys. Rev. B* **56**, 8091 (1997).

⁸T. Inami, T. Morimoto, N. Nishiyama, S. Maegawa, Y. Oka, and H. Okumura, *Phys. Rev. B* **64**, 054421/1-6 (2001).

⁹M. Nishiyama, T. Morimoto, S. Maegawa, T. Inami, and Y. Oka, *Can. J. Phys.* **79**, 1511 (2001).

¹⁰A. P. Ramirez, *Annu. Rev. Mater. Sci.* **24**, 453 (1994).

¹¹E. F. Shender and P. C. W. Holdsworth, in *Fluctuations and Order*, edited by M. Millonas (Springer-Verlag, Berlin, 1996), p. 259.

¹²J. T. Chalker, P. C. W. Holdsworth, and E. F. Shender, *Phys. Rev. Lett.* **68**, 855 (1992).

¹³J. N. Reimers and A. J. Berlinsky, *Phys. Rev. B* **48**, 9539 (1993).

¹⁴J. E. Dutrizac, *Metall. Mater. Trans. B* **14**, 531 (1983).

¹⁵A. S. Wills, V. Dupuis, E. Vincent, J. Hammann, and R. Calemczuk, *Phys. Rev. B* **62**, R9264 (2000).

¹⁶D. A. Powers, G. R. Rossman, H. J. Schugar, and H. B. Gray, *J. Solid State Chem.* **13**, 1 (1975).

¹⁷A. M. Afanasev, V. D. Gorobchenko, D. S. Kulgawczuk, and I. I. Lukashevich, *Phys. Status Solidi A* **26**, 697 (1974).

¹⁸M. Takano, T. Shinjo, M. Kiyama, and T. Takada, *J. Phys. Soc. Jpn.* **25**, 902 (1968).

¹⁹A. S. Wills, *Can. J. Phys.* **79**, 1501 (2001).

²⁰S. Maegawa, M. Nishiyama, N. Tanaka, A. Oyamada, and M. Takano, *J. Phys. Soc. Jpn.* **65**, 2776 (1996).

²¹A. Harrison, K. M. Kojima, A. S. Wills, Y. Fudamoto, M. I. Larkin, G. M. Luke, B. Nachumi, Y. J. Uemura, D. Visser, and J. S. Lord, *Physica B* **289–290**, 217 (2000).

²²G. S. Oakley, S. Pouget, A. Harrison, J. Frunzke, and D. Visser, *Physica B* **267–268**, 145 (1999).

²³G. S. Oakley, D. Visser, J. Frunzke, K. H. Andersen, A. S. Wills, and A. Harrison, *Physica B* **267–268**, 142 (1999).

²⁴A. S. Wills, A. Harrison, S. A. M. Mentink, T. E. Mason, and Z. Tun, *Europhys. Lett.* **42**, 325 (1998).

²⁵S. A. Earle, A. P. Ramirez, and R. J. Cava, *Physica B* **262**, 199 (1999).

²⁶A. Harrison, A. S. Wills, and C. Ritter, *Physica B* **241–243**, 722 (1998).

- ²⁷J. Frunzke, T. Hansen, A. Harrison, J. S. Lord, G. S. Oakley, D. Visser, and A. S. Wills, *J. Mater. Chem.* **11**, 170 (2001).
- ²⁸D. Grohol and D. G. Nocera, *J. Am. Chem. Soc.* **124**, 2640 (2002).
- ²⁹D. Papoutsakis, D. Grohol, and D. G. Nocera, *J. Am. Chem. Soc.* **124**, 2647 (2002).
- ³⁰J. L. Jambor, *Can. Mineral.* **37**, 1323 (1999).
- ³¹A. Doble, P. Y. Zavalij, and M. S. Whittingham, *Acta Crystallogr., Sect. C: Cryst. Struct. Commun.* **56**, 1294 (2000).
- ³²J. T. Szymański, *Can. Mineral.* **23**, 659 (1985).
- ³³T. Kato and Y. Miura, *Miner. Mag.* **8**, 419 (1977).
- ³⁴S. Menchetti and C. Sabelli, *Neues Jahrb. Mineral. Monatsh.*, **1976**, 406.
- ³⁵R. Wang, W. F. Bradley, and H. Steinfink, *Acta Crystallogr.* **18**, 249 (1965).
- ³⁶S. B. Hendricks, *Am. Mineral.* **22**, 773 (1937).
- ³⁷D. Grohol and D. G. Nocera (unpublished).
- ³⁸J. A. Ripmeester, C. I. Ratcliffe, J. E. Dutrizac, and J. L. Jambor, *Can. Mineral.* **24**, 435 (1986), and references therein.
- ³⁹K. Sasaki, O. Tanaike, and H. Konno, *Can. Mineral.* **36**, 1225 (1998).
- ⁴⁰K. Nakamoto, *Infrared and Raman Spectra of Inorganic and Coordination Compounds* (Wiley, New York, 1986).
- ⁴¹A. B. Harris, C. Kallin, and A. J. Berlinsky, *Phys. Rev. B* **45**, 2899 (1992).
- ⁴²A. P. Ramirez, G. P. Espinosa, and A. S. Cooper, *Phys. Rev. Lett.* **64**, 2070 (1990).
- ⁴³B. Martinez, F. Sandiumenge, A. Rouco, A. Labarta, J. Rodriguez-Carvajal, M. Tovar, M. T. Causa, S. Gali, and X. Obradors, *Phys. Rev. B* **46**, 10 786 (1992).
- ⁴⁴P. Schiffer, A. P. Ramirez, K. N. Franklin, and S.-W. Cheong, *Phys. Rev. Lett.* **77**, 2085 (1996).
- ⁴⁵H. C. Nguyen and J. B. Goodenough, *Phys. Rev. B* **52**, 324 (1995).
- ⁴⁶D. Grohol, Y. S. Lee, and D. G. Nocera (unpublished).
- ⁴⁷B. N. Figgis, *Introduction to Ligand Fields* (Interscience, New York, 1966).
- ⁴⁸F. E. Mabbs, and D. J. Machin, *Magnetism and Transition Metal Complexes* (Chapman and Hall, London, 1973).
- ⁴⁹R. L. Carlin, C. J. O'Connor, and S. N. Bhatia, *Inorg. Chem.* **15**, 985 (1976).
- ⁵⁰M. Elhajal, B. Canals, and C. Lacroix, cond-mat/0202194 (unpublished).
- ⁵¹J. B. Goodenough, *J. Phys. Chem. Solids* **6**, 287 (1958).
- ⁵²J. Kanamori, *J. Phys. Chem. Solids* **10**, 87 (1959).
- ⁵³A. P. Ginsberg, *Inorg. Chim. Acta* **5**, 45 (1971).
- ⁵⁴D. Grohol, D. Papoutsakis, and D. G. Nocera, *Angew. Chem. Int. Ed. Engl.* **40**, 1519 (2001).
- ⁵⁵L. J. DeJongh, in *Magnetic Properties of Layered Transition Metal Compounds*, edited by L. J. DeJongh (Kluwer Academic, Dordrecht, The Netherlands, 1990), p. 19.
- ⁵⁶M. Drillon, P. Panissod, P. Rabu, J. Souletie, V. Ksenofontov, and P. Gülich, *Phys. Rev. B* **65**, 104404 (2002).
- ⁵⁷D. Papoutsakis, J. P. Kirby, J. E. Jackson, and D. G. Nocera, *Chem.-Eur. J.* **5**, 1474 (1999), and references therein.
- ⁵⁸P. W. Anderson, *Science* **235**, 1196 (1987).
- ⁵⁹S. J. Clarke, A. J. Fowkes, A. Harrison, R. M. Ibberson, and M. J. Rosseinsky, *Chem. Mater.* **10**, 372 (1998).
- ⁶⁰K. Takeda, K. Miyake, K. Takeda, and K. Hirakawa, *J. Phys. Soc. Jpn.* **61**, 2156 (1992).
- ⁶¹J. Kubisz, *Miner. Pol.* **1**, 47 (1970).
- ⁶²D. M. Kurtz, Jr., *Chem. Rev.* **90**, 585 (1990).
- ⁶³O. Kahn, *Molecular Magnetism* (VCH, Weinheim, 1993).
- ⁶⁴K. Binder and A. P. Young, *Rev. Mod. Phys.* **58**, 801 (1986).
- ⁶⁵J. A. Mydosh, *Spin Glasses: An Experimental Introduction* (Taylor and Francis, London, 1993).